`deal.II` Implementation of a Two-Field Finite Element Solver for Poroelasticity

Zhuoran Wang and Jiangguo Liu[✉]

Department of Mathematics, Colorado State University, Fort Collins, CO 80523, USA
{wangz,liu}@math.colostate.edu

Abstract. This paper presents a finite element solver for poroelasticity in the 2-field approach and its implementation on the `deal.II` platform. Numerical experiments on benchmarks are presented to demonstrate the accuracy and efficiency of this new solver.

Keywords: Darcy flow · `deal.II` · Finite element methods · Hexahedral meshes · Poroelasticity · Quadrilateral meshes · Weak Galerkin

1 Introduction

Poroelasticity is an important problem in science and engineering. The Biot's model for linear poroelasticity has been well accepted and commonly used. It couples solid displacement $\mathbf{u}$ and fluid pressure p through the following partial differential equations (PDEs)

$$\begin{cases} -\nabla \cdot (2\mu\varepsilon(\mathbf{u}) + \lambda(\nabla \cdot \mathbf{u})\mathbf{I}) + \alpha\nabla p = \mathbf{f}, \\ \partial_t (c_0 p + \alpha\nabla \cdot \mathbf{u}) + \nabla \cdot (-\mathbf{K}\nabla p) = s, \end{cases} \tag{1}$$

where $\varepsilon(\mathbf{u}) = \frac{1}{2}\left(\nabla\mathbf{u} + (\nabla\mathbf{u})^T\right)$ is the strain tensor with $\lambda > 0, \mu > 0$ being the Lamé constants, $\mathbf{f}$ a given body force, $\mathbf{K}$ a conductivity tensor, s a known fluid source, α (usually close to 1) the Biot-Williams constant, and $c_0 \geq 0$ the constrained storage capacity. Appropriate boundary and initial conditions are posed to close the system.

Finite element methods (FEMs) are common tools for solving the Biot's model. Depending on the unknown quantities to be solved, poroelasticity solvers are usually grouped into 3 types:

- *2-field*: Solid displacement and fluid pressure are to be solved;
- *3-field*: Solid displacement, fluid pressure and velocity are to be solved;
- *4-field*: Solid stress & displacement, fluid pressure & velocity are to be solved.

A major issue in numerical solvers for poroelasticity is the poroelasticity locking, which usually appears as nonphysical pressure oscillations. This happens when the porous media are low-permeable or low-compressible [12,28,36].

Early on, the continuous Galerkin (CG) FEMs were applied respectively to solve for displacement and pressure. But it was soon recognized that such solvers were subject to poroelasticity locking and the 2-field approach was nearly abandoned. The mixed finite element methods can be used to solve for pressure and velocity simultaneously and meanwhile coupled with a FEM for linear elasticity that is free of Poisson-locking. Therefore, the 3-field approach has been the main stream [5,25–27,33,34]. The 4-field approach is certainly worth of investigation, but it just involves too many unknowns (degrees of freedom) [35].

The weak Galerkin (WG) finite element methods [31] have emerged as a new class of numerical methods with nice features that can be applied to a wide variety of problems including Darcy flow and linear elasticity [14,18,24,30]. Certainly, WG solvers can be developed for linear poroelasticity [17], they are free of poroelasticity locking but may involve a lot of degrees of freedom.

Recently, our efforts have been devoted to reviving the 2-field approach for development of efficient and robust finite element solvers for poroelasticity [13]. This may involve incorporation of WG FEMs with WG FEMs or classical FEMs. In this paper, we continue such efforts to develop a poroelasticity solver that couples the WG finite elements for Darcy flow and the classical Lagrangian elements with reduced integration for linear elasticity. Moreover, we provide an accessible efficient implementation of this new solver on `deal.II`, a popular finite element package [3].

2 Discretization of Linear Elasticity by Lagrangian Elements with Reduced Integration

This section discusses discretization of linear elasticity by Lagrangian Q_1^d finite elements ($d = 2, 3$) with reduced integration that is needed for our new FE solver for poroelasticity. For convenience of presentation, we consider the linear elasticity in its usual form

$$\begin{cases} -\nabla \cdot \sigma = \mathbf{f}(\mathbf{x}), \quad \mathbf{x} \in \Omega, \\ \mathbf{u}|_{\Gamma^D} = \mathbf{u}_D, \quad (\sigma \mathbf{n})|_{\Gamma^N} = \mathbf{t}_N, \end{cases} \tag{2}$$

where Ω is a 2d- or 3d-bounded domain occupied by a homogeneous and isotropic elastic body, $\mathbf{f}$ a body force, $\mathbf{u}_D, \mathbf{t}_N$ respectively Dirichlet and Neumann data, $\mathbf{n}$ the outward unit normal vector on the domain boundary that has a non-overlapping decomposition $\partial\Omega = \Gamma^D \cup \Gamma^N$. As mentioned in Sect. 1, $\mathbf{u}$ is the solid displacement, $\varepsilon(\mathbf{u}) = \frac{1}{2}\left(\nabla\mathbf{u} + (\nabla\mathbf{u})^T\right)$ the strain tensor, and $\sigma = 2\mu\,\varepsilon(\mathbf{u}) + \lambda(\nabla\cdot\mathbf{u})\mathbf{I}$ the Cauchy stress tensor with $\mathbf{I}$ being the identity matrix. The Lamé constants λ, μ are given by

$$\lambda = \frac{E\nu}{(1+\nu)(1-2\nu)}, \qquad \mu = \frac{E}{2(1+\nu)},$$

where E is the elasticity modulus and $\nu \in (0, \frac{1}{2})$ is Poisson's ratio.

One major issue in finite element solvers for linear elasticity is that as the elastic material becomes nearly incompressible or $\nu \to \frac{1}{2}$, mathematically as $\lambda \to \infty$, a FE solver may fail to produce correct results. This often appears as loss of convergence rates in displacement errors or spurious behaviors in numerical stress and dilation (divergence of displacement). This is the so-called "Poisson locking" [6]. It is well known that the classical linear (bilinear, trilinear) Lagrangian finite elements are subject to Poisson locking.

Many remedies for Poisson locking have been developed. Reduced integration is probably the easiest technique aiming at a quick fix for the classical Lagrangian elements, although the theory was less elegant [7,9,22].

In this paper, we adopt the remedy in [9] and extend it to 3-dim. In other words, we consider vector-valued Lagrangian bilinear and trilinear finite elements with reduced integration CG.Q_1^d (R.I.) (here $d = 2, 3$) for solving linear elasticity and provide `deal.II` implementation of these solvers. Specifically, the 1-point Gaussian quadrature is employed for handling the dilation term.

Let E be a convex quadrilateral with vertices $P_i(x_i, y_i)(i = 1, 2, 3, 4)$ that are oriented counterclockwise. A bilinear mapping F from $(\hat{x}, \hat{y})$ in the reference element $\hat{E} = [0, 1]^2$ to $(x, y) \in E$ is established. Its Jacobian determinant is denoted as $J(\hat{x}, \hat{y})$. On $\hat{E}$, we have 4 scalar-valued bilinear basis functions

$$
\begin{aligned}
\hat{\phi}_4(\hat{x}, \hat{y}) &= (1 - \hat{x})\hat{y}, & \hat{\phi}_3(\hat{x}, \hat{y}) &= \hat{x}\hat{y}, \\
\hat{\phi}_1(\hat{x}, \hat{y}) &= (1 - \hat{x})(1 - \hat{y}), & \hat{\phi}_2(\hat{x}, \hat{y}) &= \hat{x}(1 - \hat{y}).
\end{aligned}
\tag{3}
$$

They are mapped to the quadrilateral E as rational functions of x, y:

$$
\phi_i(x, y) = \hat{\phi}_i(\hat{x}, \hat{y}), \quad i = 1, 2, 3, 4.
\tag{4}
$$

On E, we have 8 node-based vector-valued local basis functions:

$$
\begin{bmatrix} \phi_1 \\ 0 \end{bmatrix}, \begin{bmatrix} 0 \\ \phi_1 \end{bmatrix}, \begin{bmatrix} \phi_2 \\ 0 \end{bmatrix}, \begin{bmatrix} 0 \\ \phi_2 \end{bmatrix}, \begin{bmatrix} \phi_3 \\ 0 \end{bmatrix}, \begin{bmatrix} 0 \\ \phi_3 \end{bmatrix}, \begin{bmatrix} \phi_4 \\ 0 \end{bmatrix}, \begin{bmatrix} 0 \\ \phi_4 \end{bmatrix}.
\tag{5}
$$

They span CG.$Q_1^2(E)$. The notation is a bit confusing, since the shape functions are now rationals instead of polynomials. For any $\mathbf{v} \in \text{CG}.Q_1^2(E)$, we consider

$$
\overline{\nabla \cdot \mathbf{v}} = \frac{1}{|E|} \int_E \mathbf{v}(x, y) dx dy = \frac{1}{|E|} \int_{\hat{E}} \mathbf{v}(x, y) J(\hat{x}, \hat{y}) d\hat{x} d\hat{y},
\tag{6}
$$

where $|E|$ is the volume of E.

Let $\mathbf{V}_h$ be the space of vector-valued shape functions constructed from the CG.Q_1^2 elements on a quasi-uniform quadrilateral mesh $\mathcal{E}_h$. Let $\mathbf{V}_h^0$ be the subspace of $\mathbf{V}_h$ consisting of shape functions that vanish on Γ^D. A finite element scheme for linear elasticity in the strain-div formulation seeks $\mathbf{u}_h \in \mathbf{V}_h$ so that

$$
\mathcal{A}_h^{SD}(\mathbf{u}_h, \mathbf{v}) = \mathcal{F}_h(\mathbf{v}), \quad \forall \mathbf{v} \in \mathbf{V}_h^0,
\tag{7}
$$

where

$$
\mathcal{A}_h^{SD}(\mathbf{u}_h, \mathbf{v}) = \sum_{E \in \mathcal{E}_h} 2\mu \left(\varepsilon(\mathbf{u}_h), \varepsilon(\mathbf{v}) \right)_E + \lambda (\overline{\nabla \cdot \mathbf{u}_h}, \overline{\nabla \cdot \mathbf{v}})_E,
\tag{8}
$$

$$\mathcal{F}_h(\mathbf{v}) = \sum_{E \in \mathcal{E}_h} (\mathbf{f}, \mathbf{v})_E + \sum_{\gamma \in \Gamma_h^N} \langle \mathbf{t}_N, \mathbf{v} \rangle. \tag{9}$$

3   WG Finite Element Discretization for Darcy Flow

This section briefly discusses the weak Galerkin finite element discretization for Darcy flow that is needed for our new 2-field solver for linear poroelasticity.

Among the existing finite element solvers for Darcy flow [4,8,10,11,15,18,19], [20,21,23,29,31,32], the newly developed weak Galerkin solvers have some nice features that are attractive for large-scale computing tasks. In particular, the WG($Q_k, Q_k; RT_{[k]}$) methods (with integer $k \geq 0$) approximate the primal unknown pressure by using polynomial shape function of degree at most k separately defined in element interiors and on edges/faces. Their discrete weak gradients are reconstructed in the unmapped Raviart-Thomas spaces $RT_{[k]}$ and used to approximate the classical gradient in the variational form. The WG Darcy solvers based on these novel notions

(i)   are locally mass-conservative;
(ii) provide continuous normal fluxes;
(iii) result in SPD linear systems that are easy to be solved.

In [32], we discussed `deal.II` implementation of such WG Darcy solvers for $0 \leq k \leq 5$. The numerical tests on SPE10 Model 2 have demonstrated the aforementioned nice features and practical usefulness of the novel WG methodology.

In this section, we briefly review the basic concepts of weak Galerkin by recapping WG($Q_0, Q_0; RT_{[0]}$) for Darcy flow on quadrilateral meshes. For ease of presentation, we consider the Darcy flow problem in its usual form

$$\begin{cases} \nabla \cdot (-\mathbf{K}\nabla p) \equiv \nabla \cdot \mathbf{u} = s, \\ p|_{\Gamma^D} = p_D, & \text{on } \Gamma^D \\ \mathbf{u} \cdot \mathbf{n} = u_N, & \text{on } \Gamma^N, \end{cases} \tag{10}$$

where Ω is a polygonal domain, p the primal unknown pressure, $\mathbf{u}$ the Darcy velocity, $\mathbf{K}$ conductivity tensor (medium permeability divided fluid dynamic viscosity) that is uniformly SPD over the domain, s a known source, p_D a Dirichlet boundary condition, u_N a Neumann boundary condition, $\mathbf{n}$ the outward unit normal vector on $\partial\Omega$, which has a nonoverlapping decomposition $\Gamma^D \cup \Gamma^N$.

First we define the lowest-order unmapped Raviart-Thomas space as

$$RT_{[0]}(E) = \text{Span}(\mathbf{w}_1, \mathbf{w}_2, \mathbf{w}_3, \mathbf{w}_4), \tag{11}$$

where

$$\mathbf{w}_1 = \begin{bmatrix} 1 \\ 0 \end{bmatrix}, \quad \mathbf{w}_2 = \begin{bmatrix} 0 \\ 1 \end{bmatrix}, \quad \mathbf{w}_3 = \begin{bmatrix} X \\ 0 \end{bmatrix}, \quad \mathbf{w}_4 = \begin{bmatrix} 0 \\ Y \end{bmatrix}, \tag{12}$$

and $X = x - x_c$, $Y = y - y_c$ are the normalized coordinates using the element center (x_c, y_c).

For a given quadrilateral element E, we consider 5 discrete weak functions $\phi_i(0 \leq i \leq 4)$ as follows:

- ϕ_0 for element interior: It takes value 1 in the interior E° but 0 on the boundary E^∂;
- $\phi_i (1 \le i \le 4)$ for the four sides respectively: Each takes value 1 on the i-th edge but 0 on all other three edges and in the interior.

The discrete weak gradient $\nabla_w \phi$ is established in $RT_{[0]}(E)$ via integration by parts [31]:

$$\int_E (\nabla_w \phi) \cdot \mathbf{w} = \int_{E^\partial} \phi^\partial (\mathbf{w} \cdot \mathbf{n}) - \int_{E^\circ} \phi^\circ (\nabla \cdot \mathbf{w}), \quad \forall \mathbf{w} \in RT_{[0]}(E). \qquad (13)$$

For implementation, this involves solving a size-4 SPD linear system.

However, when E becomes a rectangle $[x_1, x_2] \times [y_1, y_2]$ with $\Delta x = x_2 - x_1$, $\Delta y = y_2 - y_1$, one can obtain these discrete weak gradients explicitly:

$$\begin{cases} \nabla_w \phi_0 = & 0\mathbf{w}_1 + & 0\mathbf{w}_2 + & \frac{-12}{(\Delta x)^2}\mathbf{w}_3 + & \frac{-12}{(\Delta y)^2}\mathbf{w}_4, \\ \nabla_w \phi_1 = & \frac{-1}{\Delta x}\mathbf{w}_1 + & 0\mathbf{w}_2 + & \frac{6}{(\Delta x)^2}\mathbf{w}_3 + & 0\mathbf{w}_4, \\ \nabla_w \phi_2 = & \frac{1}{\Delta x}\mathbf{w}_1 + & 0\mathbf{w}_2 + & \frac{6}{(\Delta x)^2}\mathbf{w}_3 + & 0\mathbf{w}_4, \\ \nabla_w \phi_3 = & 0\mathbf{w}_1 + & \frac{-1}{\Delta y}\mathbf{w}_2 + & 0\mathbf{w}_3 + & \frac{6}{(\Delta y)^2}\mathbf{w}_4, \\ \nabla_w \phi_4 = & 0\mathbf{w}_1 + & \frac{1}{\Delta y}\mathbf{w}_2 + & 0\mathbf{w}_3 + & \frac{6}{(\Delta y)^2}\mathbf{w}_4. \end{cases} \qquad (14)$$

These discrete weak gradients are used to approximate the classical gradient in the variational form for the Darcy flow problem.

Let $\mathcal{E}_h$ be a quasi-uniform convex quadrilateral mesh for the given polygonal domain Ω. Let Γ_h^D be the set of all edges on the Dirichlet boundary Γ^D and Γ_h^N be the set of all edges on the Neumann boundary Γ^N. Let S_h be the space of discrete shape functions on $\mathcal{E}_h$ that are degree 0 polynomials in element interiors and also degree 0 polynomials on edges. Let S_h^0 be the subspace of functions in S_h that vanish on Γ_h^D. For (10), we seek $p_h = \{p_h^\circ, p_h^\partial\} \in S_h$ such that $p_h^\partial|_{\Gamma_h^D} = Q_h^\partial(p_D)$ (the L^2-projection of Dirichlet boundary data into the space of piecewise constants on Γ_h^D) and

$$\mathcal{A}_h(p_h, q) = \mathcal{F}(q), \qquad \forall q = \{q^\circ, q^\partial\} \in S_h^0, \qquad (15)$$

where

$$\mathcal{A}_h(p_h, q) = \sum_{E \in \mathcal{E}_h} \int_E \frac{\mathbf{K}}{\mu} \nabla_w p_h \cdot \nabla_w q, \qquad (16)$$

$$\mathcal{F}(q) = \sum_{E \in \mathcal{E}_h} \int_{E^\circ} s q^\circ - \sum_{\gamma \in \Gamma_h^N} \int_\gamma u_N q^\partial. \qquad (17)$$

Clearly, (15) is a large-size sparse SPD system.

After the numerical pressure p_h is solved from (15), an elementwise numerical velocity is obtained by a local L_2-projection back into the subspace $RT_{[0]}$:

$$\mathbf{u}_h = \mathbf{Q}_h(-\mathbf{K}\nabla_w p_h). \qquad (18)$$

The projection can be skipped if $\mathbf{K}$ is an elementwise constant scalar matrix. Furthermore, the bulk normal flux on any edge is defined as

$$\int_{e \in E^\partial} \mathbf{u}_h \cdot \mathbf{n}_e. \tag{19}$$

It has been proved [21] that such a WG solver is locally conservative and guarantees normal flux continuity.

4   Coupling $\mathrm{WG}(Q_0, Q_0; RT_{[0]})$ and $\mathrm{CG}.Q_1^2$ (R.I.) for Poroelasticity

In this section, the continuous Galerkin Q_1^d ($d = 2, 3$) elements with reduced integration and the weak Galerkin $\mathrm{WG}(Q_0, Q_0; RT_{[0]})$ elements are combined with the implicit Euler temporal discretization to solve linear poroelasticity problems.

Assume a given domain Ω is already partitioned into a quasi-uniform quadrilateral mesh $\mathcal{E}_h$. For a given time period $[0, T]$, let

$$0 = t^{(0)} < t^{(1)} < \ldots < t^{(n-1)} < t^{(n)} < \ldots < t^{(N)} = T$$

be a temporal partition. We denote $\Delta t_n = t^{(n)} - t^{(n-1)}$ for $n = 1, 2, \ldots, N$.

Let $\mathbf{V}_h$ and $\mathbf{V}_h^0$ be the spaces of vector-valued shape functions based on the first-order CG elements. Let $\mathbf{u}_h^{(n)}, \mathbf{u}_h^{(n-1)} \in \mathbf{V}_h$ be the approximations to solid displacement at time moments $t^{(n)}$ and $t^{(n-1)}$, respectively.

Let S_h and S_h^0 be the spaces of scalar-valued discrete weak functions constructed in Sect. 3 based on the $\mathrm{WG}(Q_0, Q_0; RT_{[0]})$ elements. Similarly, let $p_h^{(n)}, p_h^{(n-1)} \in S_h$ be the approximations to fluid pressure at time moments $t^{(n)}$ and $t^{(n-1)}$, respectively. Note that the discrete weak trial function has two parts:

$$p_h^{(n)} = \{p_h^{(n),\circ}, p_h^{(n),\partial}\}, \tag{20}$$

where $p_h^{(n),\circ}$ lives in element interiors and $p_h^{(n),\partial}$ lives on the mesh skeleton.

Applying the implicit Euler discretization, we establish the following time-marching scheme, for any $\mathbf{v} \in \mathbf{V}_h^0$ and any $q \in S_h^0$,

$$\begin{cases} 2\mu\Big(\varepsilon(\mathbf{u}_h^{(n)}), \varepsilon(\mathbf{v})\Big) + \lambda(\overline{\nabla \cdot \mathbf{u}_h^{(n)}}, \overline{\nabla \cdot \mathbf{v}}) - \alpha(p_h^{(n),\circ}, \overline{\nabla \cdot \mathbf{v}}) = (\mathbf{f}^{(n)}, \mathbf{v}), \\ c_0\Big(p_h^{(n),\circ}, q^\circ\Big) + \Delta t_n\Big(\mathbf{K}\nabla p_h^{(n)}, \nabla q\Big) + \alpha(\overline{\nabla \cdot \mathbf{u}_h^{(n)}}, q^\circ) \\ \qquad = c_0\Big(p_h^{(n-1),\circ}, q^\circ\Big) + \Delta t_n\Big(s^{(n)}, q^\circ\Big) + \alpha(\overline{\nabla \cdot \mathbf{u}_h^{(n-1)}}, q^\circ), \end{cases} \tag{21}$$

for $n = 1, 2, \ldots, N$, where $\overline{\nabla \cdot \mathbf{v}}$ is the elementwise average that represents the reduced integration technique. The above two equations are further augmented with appropriate boundary and initial conditions. This results in a large monolithic system at each time step.

Theses errors are calculated to assess the accuracy of our poroelasticity solver:

- $L_2([0,T]; L_2(\Omega))$-**norm for interior pressure errors**

$$\|p - p_h^\circ\|_{L_2(L_2)}^2 = \sum_{n=1}^{N} \Delta t_n \|p^{(n)} - p_h^{((n),\circ)}\|_{L_2(\Omega)}^2, \tag{22}$$

- $L_2([0,T]; L_2(\Omega))$-**norm for displacement errors**

$$\|\mathbf{u} - \mathbf{u}_h\|_{L_2(L_2)}^2 = \sum_{n=1}^{N} \Delta t_n \|\mathbf{u}^{(n)} - \mathbf{u}_h^{(n)}\|_{L_2(\Omega)}^2, \tag{23}$$

- $L_2([0,T]; H^1(\Omega))$-**norm for displacement errors**

$$\|\mathbf{u} - \mathbf{u}_h\|_{L_2(H^1)}^2 = \sum_{n=1}^{N} \Delta t_n \|\nabla\mathbf{u}^{(n)} - \nabla\mathbf{u}_h^{(n)}\|_{L_2(\Omega)}^2, \tag{24}$$

- $L_2([0,T]; L_2(\Omega))$-**norm for stress errors**

$$\|\sigma - \sigma_h\|_{L_2(L_2)}^2 = \sum_{n=1}^{N} \Delta t_n \|\sigma^{(n)} - \sigma_h^{(n)}\|_{L_2(\Omega)}^2. \tag{25}$$

5   Code Excerpts with Comments

This section provides some code excerpts with comments. More details can be found in our code modules for `deal.II` (subject to minor changes). We want to point that the elasticity discretization can also be replaced by the so-called EQ_1 or BR_1 elements [3,16], which are now available in `deal.II` Version 9.1.

5.1   Code Excerpts for WG($Q_0, Q_0; RT_{[0]}$)

There was a discussion on this in [32]. Here we recap the most important concepts very briefly. Note that `FE_RaviartThomas` is a Raviart-Thomas space for vector-valued functions, `FESystem` defines WG finite element spaces in the interiors and on edges/faces. Shown below is the code for the lowest-order WG finite elements.

```
88   FE_RaviartThomas<dim> fe_rt;
89   DoFHandler<dim> dof_handler_rt;
90   FESystem<dim> fe;
91   DoFHandler<dim> dof_handler;
```

```
227   fe_rt (0);
228   dof_handler_rt (triangulation);
229   fe (FE_DGQ<dim>(0), 1, FE_FaceQ<dim>(0), 1);
230   dof_handler (triangulation);
```

5.2   Code Excerpts for CG.Q_1^2 with Reduced Integration

This part shows how we use CG.Q_1^2 with reduced integration to discretize linear elasticity. **FE_Q** defines the finite element space for displacement vectors. Each component of the vector is in the **FE_Q** space.

```
88   FE_Q<dim>(1),dim;
```

Here, the reduced integration technique with one-point Gaussian quadrature is used to calculate the dilation (divergence of displacement).

```
88   QGauss<dim>  reduced_integration_quadrature_formula(1);
```

5.3   Code Excerpts for Coupled Discretizations for Poroelasticity

We couple CG.Q_1^2(R.I.) and WG($Q_0, Q_0; RT_{[0]}$) to solve linear poroelasticity. **FESystem** defines the finite element spaces for displacement, interior pressure, and face pressure. Shown below is the coupled finite elements.

```
88   FE_RaviartThomas<dim>  fe_rt;
89   DoFHandler<dim>        dof_handler_rt;
90   FESystem<dim>              fe;
91   DoFHandler<dim>        dof_handler;
```

```
88   fe_rt (0),
89   dof_handler_rt (triangulation),
90
91   fe (FE_Q<dim>(1),dim,
92      FE_DGQ<dim>(0), 1,
93      FE_FaceQ<dim>(0), 1),
94   dof_handler (triangulation),
```

We use block structures to store matrices and variables. The following piece defines the degrees of freedom associated with displacement, interior pressure, and face pressure.

```
88   std::vector<types::global_dof_index> dofs_per_block (3);
89   DoFTools::count_dofs_per_block
90   (dof_handler, dofs_per_block, block_component);
91   const unsigned int n_u = dofs_per_block[0],
92                  n_p_interior = dofs_per_block[1],
93                  n_p_face =  dofs_per_block[2],
94                  n_p = dofs_per_block[1]+ dofs_per_block[2];
```

The implementation for the WG Darcy solver discussed in [32] is naturally re-used and incorporated. The following piece calculates the coupling terms with reduced integration in the local matrix. However, we only use the reduced integration for divergence of vector-valued shape functions.

```
88  for (unsigned int q_index = 0;
89       q_index < n_q_points_reduced_integration; ++q_index){
90   for (unsigned int i = 0; i < dofs_per_cell; ++i){
91    const double div_i_reduced_integration =
92    fe_values_reduced_integration
93     [displacements_reduced_integration].divergence(i, q_index);
94     for (unsigned int j = 0; j < dofs_per_cell; ++j){
95      const double div_j_reduced_integration =
96      fe_values_reduced_integration
97      [displacements_reduced_integration].divergence(j, q_index);
98
99      local_matrix(i, j) +=
100     - alpha * fe_values_reduced_integration
101      [pressure_interior_reduced_integration].value(j, q_index)
102     * div_i_reduced_integration
103      + alpha* (div_j_reduced_integration
104      * fe_values_reduced_integration
105     [pressure_interior_reduced_integration].value (i,q_index)))
106      * fe_values_reduced_integration.JxW(q_index);
107 }}}
```

Finally, this piece hands the coupling term in the local right-hand side.

```
88  for (unsigned int q=0; q<n_q_points_reduced_integration; ++q){
89    for (unsigned int i=0; i<dofs_per_cell; ++i){
90      const double phi_i_q =
91        fe_values_reduced_integration
92          [pressure_interior_reduced_integration].value(i,q);
93        local_rhs(i) +=
94          (alpha*div_old_displacement_reduced_integration[q]
95          * phi_i_q
96          * fe_values_reduced_integration.JxW(q);
97 }}
```

6   Numerical Experiments

This section presents numerical examples to demonstrate the accuracy and robustness of this new finite element solver for poroelasticity.

Example 1 (A 2-dim smooth example for convergence rates). Here our domain is $\Omega = (0,1)^2$. Analytical solutions for solid displacement and fluid pressure are given as

$$\mathbf{u} = \sin\left(\frac{\pi}{2}t\right) \begin{bmatrix} \dfrac{\pi}{2}\sin^2(\pi x)\sin(2\pi y) + \dfrac{1}{\lambda}\sin(\pi x)\sin(\pi y) \\ -\dfrac{\pi}{2}\sin(2\pi x)\sin^2(\pi y) + \dfrac{1}{\lambda}\sin(\pi x)\sin(\pi y) \end{bmatrix}, \qquad (26)$$

$$p = \frac{\pi}{\lambda}\sin\left(\frac{\pi}{2}t\right)\sin(\pi(x+y)). \qquad (27)$$

It is interesting to see that

$$\nabla \cdot \mathbf{u} = p, \qquad (28)$$

and hence $\nabla \cdot \mathbf{u} \to 0$ as $\lambda \to \infty$. Dirichlet boundary conditions for both displacement and pressure are specified on the whole boundary using the exact solutions. For the parameters, we have $\mathbf{K} = \kappa\mathbf{I}$ with $\kappa = 1$, $\mu = 1$, $\alpha = 1$, and $c_0 = 0$. To examine the solver's locking-free property, we shall consider $\lambda = 1$ and $\lambda = 10^6$, respectively. The time period is $[0, T] = [0, 1]$.

For numerical simulations, we consider uniform rectangular meshes. Shown in Tables 1 and 2 are the numerical results obtained with this new solver. Clearly, the convergence rates do not deteriorate as λ increases from 1 to 10^6. In other words, our new 2-field solver is locking-free.

Table 1. Ex.1 with $\lambda = 1$: Numerical results of $\mathrm{CG}.Q_1^2(\mathrm{R.I.}) + \mathrm{WG}(Q_0, Q_0; RT_{[0]})$ solver on rectangular meshes

$1/h$	$1/\Delta t$	$\|p - p_h^\circ\|_{L_2(L_2)}$	$\|\mathbf{u} - \mathbf{u}_h\|_{L_2(L_2)}$	$|\mathbf{u} - \mathbf{u}_h|_{L_2(H^1)}$	$\|\sigma - \sigma_h\|_{L_2(L_2)}$
4	16	5.07478E−1	1.78798E−1	2.35598E−0	4.44080E−0
8	64	2.52365E−1	4.54880E−2	1.15497E−0	2.29855E−0
16	256	1.25983E−1	1.14071E−2	5.74435E−1	1.15784E−0
32	1024	6.29657E−2	2.85375E−3	2.86836E−1	5.79949E−1
Conv. rate		1.00	1.98	1.01	0.97

Example 2 (A 3-dim example with a sandwiched low permeability layer). The domain is the unit cube $\Omega = (0,1)^3$. The permeability is $\mathbf{K} = \kappa\mathbf{I}$. Specifically, the middle region $0.25 \le z \le 0.75$ has a low permeability $\kappa = 10^{-8}$, whereas $\kappa = 1$ in other parts, see Fig. 1(a). There is no body force for solid or source for fluid. Other parameters are $\lambda = 1$, $\mu = 1$, $\alpha = 1$, $c_0 = 0$.

The boundary conditions are as follows.

(i) For the solid, a downward traction (Neumann) condition $\mathbf{t}_N = (0, 0, -1)^T$ is posed on the top face, whereas all five other faces are clamped, i.e., $\mathbf{u} = \mathbf{0}$;

Table 2. Ex.1 with $\lambda = 10^6$: Numerical results of $CG.Q_1^2(R.I.) + WG(Q_0, Q_0; RT_{[0]})$ solver on rectangular meshes

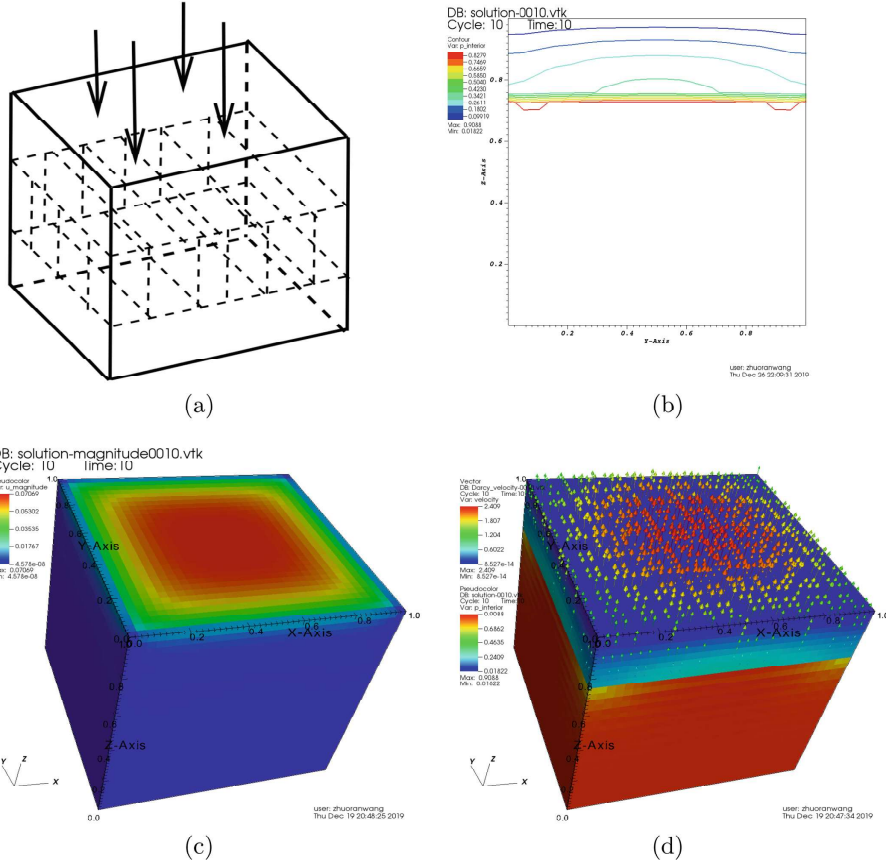| $1/h$	$1/\Delta t$	$\|p - p_h^\circ\|_{L_2(L_2)}$	$\|\mathbf{u} - \mathbf{u}_h\|_{L_2(L_2)}$	$|\mathbf{u} - \mathbf{u}_h|_{L_2(H^1)}$	$\|\sigma - \sigma_h\|_{L_2(L_2)}$
4	16	5.07481E−7	1.76096E−1	2.30126E−0	1.36770E+6
8	64	2.52367E−7	4.48677E−2	1.12759E−0	7.66388E+5
16	256	1.25984E−7	1.12553E−2	5.60529E−1	3.92554E+5
32	1024	6.29658E−8	2.81600E−3	2.79849E−1	1.97411E+5
Conv. rate		1.00	1.98	1.01	0.93

(a)

(b)

(c)

(d)

Fig. 1. Ex.2: Numerical results from the new FE solver at final time $T = 0.01$ with $h = 1/32$ and $\Delta t = 10^{-3}$. (a) Problem illustration; (b) Numerical pressure contours for $x = 0.5$; (c) Numerical displacement magnitude elementwise average; (d) Numerical pressure cell averages and velocity at element centers.

(ii) For the fluid, the top face ($z = 1$) has a Dirichlet condition $p = 0$; whereas all five other faces have a no-flow condition, in other words, zero Neumann boundary condition.

A similar 2-dim problem has been tested in [12,13,17]. But we shall observe richer features in this 3-dim problem.

For numerical simulations, we use uniform rectangular meshes and a uniform temporal partition. Specifically, $h = \frac{1}{32}$ and $\Delta t = 10^{-3}$ so that $\Delta t \approx h^2$. The final time is $T = 0.01$, which means 10 time steps for simulation. Shown in Fig. 1 are the profiles of numerical pressure and velocity along with solid displacement magnitude. There is no pressure oscillation, even though there is a layer with a very low permeability. A pressure steep front is observed near $z = 0.75$. The low permeability layer provides some kind of insulation. There is basically no solid deformation or fluid pressure change below this layer.

7   Concluding Remarks

A new finite element solver for poroelasticity is presented and proven numerically to be locking-free. This new solver is in the 2-field approach, i.e., only solid displacement and fluid pressure are treated as unknowns. Specifically, the new solver discretizes displacement using the classical Lagrangian Q-type elements with reduced integration, whereas the pressure is approximated by piecewise constants respectively defined inside elements and on inter-element boundaries. Discrete weak gradients of such piecewise constant shape functions are established in the unmapped lowest-order Raviart-Thomas spaces on quadrilaterals and hexahedra, which are required to be asymptotically parallelogram or parallelopiped. This new solver has been implemented in the dimension-independent paradigm on the deal.II platform. Our code modules are openly accessible.

The new solver in this paper is different than the one presented in [13]. Now the elasticity part is discretized using the classical Lagrangian Q-type elements with reduced integration. This results in even less degrees of freedom.

There are several directions one can go from here.

  (i) Code optimization, especially, preconditioning and parallelization, shall make this new solver more efficient;
 (ii) A rigorous analysis on this new solver is to be established for the locking-free property and convergence rates;
(iii) A similar solver can be developed for simplicial (triangular and tetrahedral) meshes; Implementation on FEniCS or FreeFEM++ platforms are surely attractive for scientific computing tasks;
(iv) To remove the restriction *asymptotically parallelogram or parallelopiped*, we could utilize the newly developed Arbogast-Correa and Abogast-Tao elements [1,2] for more general convex quadrilaterals and cuboidal hexahedra. Again deal.II implementation will be attractive.

These are under our investigation and will be reported in our future work.

References

1. Arbogast, T., Correa, M.: Two families of mixed finite elements on quadrilaterals of minimal dimension. SIAM J. Numer. Anal. **54**, 3332–3356 (2016)
2. Arbogast, T., Tao, Z.: Construction of H(div)-conforming mixed finite elements on cuboidal hexahedra. Numer. Math. **142**, 1–32 (2019)
3. Arndt, D., et al.: The `deal.II` library, version 9.1. J. Numer. Math. (2019). https://doi.org/10.1515/jnma-2019-0064. https://dealii.org/deal91-preprint.pdf
4. Bastian, P., Riviere, B.: Superconvergence and $H(div)$ projection for discontinuous Galerkin methods. Int. J. Numer. Meth. Fluids **42**, 1043–1057 (2003)
5. Berger, L., Bordas, R., Kay, D., Tavener, S.: Stabilized lowest-order finite element approximation for linear three-field poroelasticity. SIAM J. Sci. Comput. **37**, A2222–A2245 (2015)
6. Brenner, S., Scott, L.: The Mathematical Theory of Finite Element Methods, Texts in Applied Mathematics, vol. 15, 3rd edn. Springer, New York (2008)
7. Brenner, S., Sung, L.Y.: Linear finite element methods for planar linear elasticity. Math. Comput. **59**, 321–338 (1992)
8. Bush, L., Ginting, V.: On the application of the continuous Galerkin finite element method for conservation problems. SIAM J. Sci. Comput. **35**, A2953–A2975 (2013)
9. Cheng, X., Huang, H., Zou, J.: Quadrilateral finite elements for planar linear elasticity problem with large Lamé constant. J. Comput. Math. **16**, 357–366 (1998)
10. Cockburn, B., Gopalakrishnan, J., Wang, H.: Locally conservative fluxes for the continuous Galerkin method. SIAM J. Numer. Anal. **45**, 1742–1770 (2007)
11. Brezzi, F., Fortin, M.: Mixed and Hybrid Finite Element Methods. Springer, New York (1991). https://doi.org/10.1007/978-1-4612-3172-1
12. Haga, J., Osnes, H., Langtangen, H.: On the causes of pressure oscillations in low permeable and low compressible porous media. Int. J. Numer. Anal. Meth. Geomech. **36**, 1507–1522 (2012)
13. Harper, G., Liu, J., Tavener, S., Wang, Z.: A two-field finite element solver for poroelasticity on quadrilateral meshes. In: Shi, Y., Fu, H., Tian, Y., Krzhizhanovskaya, V.V., Lees, M.H., Dongarra, J., Sloot, P.M.A. (eds.) ICCS 2018. LNCS, vol. 10862, pp. 76–88. Springer, Cham (2018). https://doi.org/10.1007/978-3-319-93713-7_6
14. Harper, G., Liu, J., Tavener, S., Zheng, B.: Lowest-order weak Galerkin finite element methods for linear elasticity on rectangular and brick meshes. J. Sci. Comput. **78**, 1917–1941 (2019)
15. Harper, G., Liu, J., Zheng, B.: The THex algorithm and a simple Darcy solver on hexahedral meshes. Proc. Comput. Sci. **108C**, 1903–1912 (2017)
16. Harper, G., Wang, R., Liu, J., Tavener, S., Zhang, R.: A locking-free solver for linear elasticity on quadrilateral and hexahedral meshes based on enrichment of Lagrangian elements. Technical report, Colorado State University (2020)
17. Hu, X., Mu, L., Ye, X.: Weak Galerkin method for the Biot's consolidation model. Comput. Math. Appl. **75**, 2017–2030 (2018)
18. Lin, G., Liu, J., Mu, L., Ye, X.: Weak Galerkin finite element methdos for Darcy flow: anistropy and heterogeneity. J. Comput. Phys. **276**, 422–437 (2014)
19. Liu, J., Sadre-Marandi, F., Wang, Z.: Darcylite: a matlab toolbox for Darcy flow computation. Proc. Comput. Sci. **80**, 1301–1312 (2016)
20. Liu, J., Tavener, S., Wang, Z.: Lowest-order weak Galerkin finite element method for Darcy flow on convex polygonal meshes. SIAM J. Sci. Comput. **40**, B1229–B1252 (2018)

21. Liu, J., Tavener, S., Wang, Z.: The lowest-order weak Galerkin finite element method for the Darcy equation on quadrilateral and hybrid meshes. J. Comput. Phys. **359**, 312–330 (2018)
22. Malkus, D.S., Hughes, T.: Mixed finite element methods - reduced and selective integration techniques: a unification of concepts. Comput. Meth. Appl. Mech. Eng. **15**, 63–81 (1978)
23. Mu, L., Wang, J., Ye, X.: A weak Galerkin finite element method with polynomial reduction. J. Comput. Appl. Math. **285**, 45–58 (2015)
24. Mu, L., Wang, J., Ye, X.: Weak Galerkin finite element methods on polytopal meshes. Int. J. Numer. Anal. Model. **12**, 31–53 (2015)
25. Phillips, P., Wheeler, M.: A coupling of mixed with continuous Galerkin finite element methods for poroelasticity I: the continuous in time case. Comput. Geosci. **11**, 131–144 (2007)
26. Phillips, P., Wheeler, M.: A coupling of mixed with continuous Galerkin finite element methods for poroelasticity II: the-discrete-in-time case. Comput. Geosci. **11**, 145–158 (2007)
27. Phillips, P., Wheeler, M.: A coupling of mixed with discontinuous Galerkin finite element methods for poroelasticity. Comput. Geosci. **12**, 417–435 (2008)
28. Phillips, P.J., Wheeler, M.F.: Overcoming the problem of locking in linear elasticity and poroelasticity: an heuristic approach. Comput. Geosci. **13**, 5–12 (2009)
29. Sun, S., Liu, J.: A locally conservative finite element method based on piecewise constant enrichment of the continuous Galerkin method. SIAM J. Sci. Comput. **31**, 2528–2548 (2009)
30. Wang, C., Wang, J., Wang, R., Zhang, R.: A locking-free weak Galerkin finite element method for elasticity problems in the primal formulation. J. Comput. Appl. Math. **307**, 346–366 (2016)
31. Wang, J., Ye, X.: A weak Galerkin finite element method for second order elliptic problems. J. Comput. Appl. Math. **241**, 103–115 (2013)
32. Wang, Z., Harper, G., O'Leary, P., Liu, J., Tavener, S.: `deal.II` implementation of a weak galerkin finite element solver for Darcy flow. In: Rodrigues, J.M.F., et al. (eds.) ICCS 2019. LNCS, vol. 11539, pp. 495–509. Springer, Cham (2019). https://doi.org/10.1007/978-3-030-22747-0_37
33. Wheeler, M., Xue, G., Yotov, I.: Coupling multipoint flux mixed finite element methods with continuous Galerkin methods for poroelasticity. Comput. Geosci. **18**, 57–75 (2014)
34. Yi, S.Y.: A coupling of nonconforming and mixed finite element methods for Biot's consolidation model. Numer. Meth. PDEs **29**, 1749–1777 (2013)
35. Yi, S.Y.: Convergence analysis of a new mixed finite element method for Biot's consolidation model. Numer. Meth. PDEs **30**, 1189–1210 (2014)
36. Yi, S.Y.: A study of two modes of locking in poroelasticity. SIAM J. Numer. Anal. **55**, 1915–1936 (2017)